interaction could result in the formation of more potassium phosphate in flue gas during the co–combustion of coal with secondary fuels, compared with coal combustion (Zhuo *et al.*, 2012). Potassium phosphate will be deposited on the surface of SCR catalysts and unavoidably have a further effect on their activities. Because of practical interests, quite a few researchers have investigated the influence of K_3PO_4 on V_2O_5/TiO_2 based catalysts (Beck *et al.*, 2004; Castellino *et al.*, 2009). However, the effect of K_3PO_4 on ceria–based catalysts has been ignored and hardly ever studied until our present work. In addition, different K species would exert a different effect on catalytic behaviors (Zhang *et al.*, 2015; Du *et al.*, 2017). Consequently, it is indispensable to further investigate the effect of K_3PO_4 on the SCR of NO with NH_3 over Ce–Ti oxide catalyst. These catalysts were characterized by means of BET, XRD, XPS, NH_3–TPD, H_2–TPR and catalytic activity measurements in this work.

2. Experimental

2.1 Catalyst preparation

Ce–Ti oxide was prepared by a single step sol–gel method and denoted as CT. The CeO_2 loading was set to 20% (the mass ratio of CeO_2/TiO_2). Butyl titanate (0.1mol), anhydrous ethanol (3.5 mol), deionized water (1.9 mol), nitric acid (0.2 mol) and cerium nitrate (0.01mol) were mixed and stirred violently at room temperature. After 3 h, the mixture was dried at 80 ºC for 24 h to form xerogel. At last, the xerogel was calcined at 500 ºC for 6 h.

The K_3PO_4– and H_3PO_4–doped catalysts were prepared by impregnation via incipient wetness with the aqueous solutions of required concentrations of K_3PO_4 and

87 H_3PO_4 on the Ce–Ti oxide, respectively. The samples were impregnated at room
88 temperature for 4 h. Then the samples were dried at 110 ºC for 12 h. As for the
89 P_2O_5–doped catalyst, H_3PO_4 was used as the precursor of P_2O_5 and impregnated on
90 the Ce–Ti oxide at home temperature for 4 h. After died at 110 ºC for 12 h, the sample
91 was calcined at 500 ºC for 5 h. A series of K_3PO_4–doped samples were denoted by
92 KPCT(x) and x was the molar ratio of K to Ce.

93 2.2 Characterization of catalysts

94 The physical properties of the samples were measured by N_2 adsorption and
95 desorption at 77 K with ASAP 2020–M (Micromeritics Instrument Corp.). According
96 to the Brunauer–Emmett–Teller (BET) and Barrett–Joyner–Halenda (BJH) methods,
97 BET surface area, total pore volume and average pore diameter could be determined.

98 X–ray diffraction (XRD) patterns were obtained on an X'Pert PRO MPD system
99 (Panalytical Corp.) with Cu Kα radiation operating at 40 kV and 40 mA. The XRD
100 data were collected in the scattering angles (2θ) ranging between 10 and 90° with a
101 scanning rate of 5º/min.

102 The X–ray photoelectron spectroscopy (XPS) spectra were collected on a
103 Thermo ESCALAB 250 spectrometer using monochromated Al Kα X–rays radiation
104 ($h\nu$=1486.6 eV) at 150 W. The binding energies of K 2p, Ti 2p, Ce 3d and O 1s were
105 calibrated by measuring the reference peak of C 1s (BE=284.6 eV) from adventitious
106 carbon in order to eliminate sample charging effect.

107 The analysis on temperature programmed desorption (NH_3–TPD) and
108 temperature programmed reduction (H_2–TPR) were carried out on a

FINESORB–3010 chemisorption analyzer (FINETEC Instruments Corp.) with a thermal conductivity detector (TCD).

2.3 Catalytic activity tests

The SCR activities of the samples were tested in a fixed–bed quartz tubular flow reactor (i.d. 8mm) containing 0.34 g catalyst with 60–100 mesh in the temperature range of 150–500 ºC. The feed gas consisted of 1000 ppm NO, 1000 ppm NH_3, 3% O_2 and balance N_2. The total flow rate was 500 mL/min, corresponding to a gas hourly space velocity (GHSV) was 90,000 h^{-1}. The concentrations of NO and O_2 were monitored by a flue gas analyzer (350 Pro, Testo). The concentrations of NH_3, N_2O and NO_2 were analyzed by a FT–IR gas analyzer (DX–4000, Gasmet). The activity data were collected and recorded after 30 min when the SCR reaction reached a steady state at each temperature.

3. Results and discussion

3.1 SCR activity tests

Fig. 1 compares NO conversion as a function of temperatures over Ce–Ti oxides doped with different P species. As for H_3PO_4– and P_2O_5–doped samples, the molar ratio of P/Ce was 0.5:1. Over CT–K_3PO_4, the molar ratio of K/P/Ce was 0.5:0.2:1. It could be seen that the deactivation of CT followed the sequence: CT–P_2O_5<CT–H_3PO_4<CT–K_3PO_4. It was clear that different P species would exert a different effect on catalytic behaviors of CT. K_3PO_4 led to most serious deactivation of CT compared with the other two P species. After that, the effect of K_3PO_4 loadings on the catalytic behaviors of CT was investigated and the results are shown in Fig. 2.

131 The catalytic activity of CT deceased with increasing K_3PO_4 loadings in the
132 temperature range of 150–500 ºC. When the molar ratio of K/Ce reached 0.25, the
133 maximum NO conversion fell to only less than 30% and CT had lost most of its
134 activity. These results indicated that K_3PO_4 acted as a strong inhibitor on the catalytic
135 activity of CT.

136 The oxidation activities of NO to NO_2 by O_2 were measured over the fresh CT
137 and KPCT(0.5) and the results are presented Fig. 3. As for the fresh CT, the NO
138 oxidation increased with increasing temperatures and reached the maximum of 13.9%
139 at 450 ºC. Further increasing temperatures led to the drop in the NO oxidation. After
140 adding K_3PO_4, the NO oxidation decreased obviously. It is established that the
141 existence of NO_2 can promote the SCR reaction via the "fast SCR reaction" of
142 $2NH_3+NO+NO_2 \rightarrow 2N_2+3H_2O$ (Fedeyko *et al.*, 2010; Ma *et al.*, 2013). It implied that
143 K_3PO_4 could inhibited the oxidation of NO to NO_2, thereby decreasing the SCR
144 activity of CT.

145 NH_3 oxidation, as an important side reaction, can cause the decrease in SCR
146 activity at high temperatures (Ma *et al.*, 2013). NH_3 oxidation tests were performed in
147 the feed gas without NO. The concentrations of N_2O and NO_2 were lower than 7 ppm
148 over the two samples in the temperature range of 150–500 ºC. Therefore, the NH_3
149 oxidation results only contained the NO concentration curves (see Fig. 4). It could be
150 seen from Fig. 4 that the NH_3 oxidation started at about 350 ºC and increased sharply
151 with temperatures over the fresh CT. After doping K_3PO_4, NO concentration increased
152 at 350–500 ºC obviously, while no obvious change was observed below 350 ºC. This

153 indicated that the presence of K_3PO_4 could resulted in the formation of more NO at
154 high temperatures, which led to the decrease in the SCR activity of CT.

155 3.2 Characterization of catalysts

156 3.2.1 XRD results

157 The XRD patterns of Ce–Ti oxides with various K_3PO_4 loadings are illustrated in
158 Fig. 5. For the fresh CT, only anatase TiO_2 could be detected while the characteristic
159 diffraction peaks of Ce species were not found. This indicated that Ce species were
160 well dispersed and existed as an amorphous or highly dispersed phase on the surface
161 of anatase TiO_2. After doping K_3PO_4, the characteristic peaks belonging to Ce, K or P
162 species were not observed. Du *et al.* (2012) found similar phenomena when they
163 studied the effect of K and Na on Ce–Ti oxide prepared by a co–precipitation method.
164 It meant that the dispersion of CeO_2 was barely influenced by K_3PO_4. However, the
165 intensity of the characteristic peaks of anatase TiO_2 was found to decrease over
166 KPCT(0.5). Our previous study found a similar phenomenon over Ca–doped Ce–Ti
167 oxide catalysts (Jiang *et al.*, 2017b). The mean crystallite size of anatase was
168 evaluated using the Scherrer equation. When the molar ratio of K/Ce was lower than
169 0.5, the grain size of anatase was about 4.8 nm. As for KPCT(0.5), the grain size of
170 anatase decreased to 3.4 nm. The mean crystallite sizes of anatase in different samples
171 agreed well with the XRD results. It indicated that there existed a strong interaction
172 between K_3PO_4 and TiO_2.

173 3.2.2 N_2 adsorption–desorption results

174 Fig. 6 shows the N_2 adsorption–desorption isotherms and corresponding pore size

distribution curves of the fresh and K_3PO_4–doped CT catalysts. Both samples had a typical "IV" isotherm, suggestive of mesoporous structures (Leofantia, *et al*., 1998). As shown in Fig. 6(b), the pore distribution of the fresh CT was centered at around 6.2 nm, attributed to the pore structure of the TiO_2 support. After doping K_3PO_4, the pore size was slightly shifted to a higher value while the pore volume decreased a little. It confirmed that the impregnation of K_3PO_4 only caused slight pore blocking.

3.2.3 XPS results

Table 1 lists the concentration of various atoms on the fresh and K_3PO_4–doped CT catalysts. The presence of K_3PO_4 resulted in the slight decrease in the concentration of active Ce atom from 30.53 at.% to 30.18 at.%. The concentrations of Ti and O were also found to fell, compared with those on the surface of the fresh CT. It seemed probably to be originated from the fact that the catalyst surface might be covered with K_3PO_4 during its impregnation process. K_3PO_4 hindered the XPS detection of Ce, Ti and O atoms, which lied under K_3PO_4. In our previous study on the effect of $PbCl_2$ on V_2O_5/TiO_2, similar phenomena were also observed (Jiang *et al.*, 2014).

Fig. 7 shows XPS spectra of K 2p, Ti 2p, Ce 3d and O 1s. As shown in Fig. 7(a), the binding energy of the $2p_{3/2}$ peak was 293.2 eV in the K 2p XPS spectra of KPCT(0.5). Referring to the handbook of XPS (Wagner, *et al.*, 1979), it could be inferred that K existed in the form of K_3PO_4 on the surface of KPCT(0.5).

For the fresh CT, two main peaks ascribed to Ti $2p_{1/2}$ and Ti $2p_{3/2}$ were observed at about 464.5 eV and 458.4 eV, respectively (see Fig. 7(b)). It indicated that Ti was

present in the form of Ti^{4+} (Wagner, *et al.*, 1979). After doping K_3PO_4, the binding energies of Ti 2p were hardly changed. It implied that the presence of K_3PO_4 had almost no impact on the chemical state of Ti. Ti still existed as Ti^{4+} in KPCT(0.5). However, the intensity of the Ti 2p XPS peaks was found to decrease to a certain extent. This might be ascribed to an interaction between K_3PO_4 and Ti, which was also demonstrated in XRD results.

According to the convention established by Burroughs *et al.* (1976), the XPS spectra of Ce 3d could be deconvoluted into eight overlapped peaks. The peaks labeled as *u′* and *v′* represented the $3d^{10}4f^{1}$ initial electronic state corresponding to surface Ce^{3+}, while the other ones were assigned to the $3d^{10}4f^{0}$ initial electronic state of surface Ce^{4+} species (Burroughs, *et al.*, 1976). As exhibited in Fig. 7 (c), Ce existed in both forms of Ce^{3+} and Ce^{4+} on the surface of the fresh CT. It is widely accepted that the Ce^{3+}/Ce^{4+} pairs contribute to the storage and release of active oxygen species and the oxidation of NO to NO_2 (Geng *et al.*, 2017). Furthermore, higher Ce^{3+} ratio are indicative of more oxygen vacancies, which help to adsorb reactants (Liu *et al.*, 2013a; Liu *et al.*, 2013b). All of these factors are favorable to the SCR reaction. According to the area ratio of peaks ascribed to Ce^{3+} and Ce^{4+}, the ratio of $Ce^{3+}/(Ce^{3+}+Ce^{4+})$ could be calculated. After doping K_3PO_4, the ratio of $Ce^{3+}/(Ce^{3+}+Ce^{4+})$ decreased from 0.48 to 0.29. It was clear that the amount of Ce^{3+} decreased after doping K_3PO_4. The oxidation state of Ce species on the catalyst surface was changed remarkably. The decrease in the amount of Ce^{3+} resulted from the fact that the interaction between K_3PO_4 and Ce species suppressed the reduction of

219 Ce^{4+} to Ce^{3+} in SCR reaction. Consequently, the reducibility of the CT was lessened.
220 In addition, K_3PO_4 acted as an inhibitor on the electron transfer and resulted in the
221 decrease in the amount of oxygen vacancies, which was disadvantageous to the
222 adsorption and activation of reactive species (Geng *et al*., 2017). In a word, the
223 decrease in the amount of Ce^{3+} and the degradation of reducibility should be
224 responsible for a strong inhibition of K_3PO_4 in the activity of the Ce–Ti oxide.

225 The O 1s XPS curves of different samples were made up of three overlap peaks,
226 as illustrated in Fig. 7(d). The peaks at 527.7–530.6 eV corresponded to lattice oxygen
227 O^{2-} in the metal oxides (denoted as O_α), the peaks at 530.6–531.1 eV belonged to
228 surface labile oxygen such as O^- or OH from defect-oxide or hydroxyl–like groups
229 (denoted as O_β), and the peaks at 531.1–533.5 eV were assigned as chemisorbed water
230 (denoted as O_γ) (Dupin *et al.*, 2000; Eom *et al.*, 2008; Lee and Bai, 2018). Owing to
231 its higher mobility, O_β is considerably more active than O_α and O_γ (Jiang *et al.*, 2018).
232 High O_β ratio is beneficial for the oxidation of more NO to NO_2 in the SCR process
233 (Wu *et al.*, 2008; Chen *et al.*, 2009). It was reported that the reaction rate of NH_3 with
234 the mixture of NO and NO_2 was be faster than that with NO alone, especially at low
235 temperature (Long and Yang, 1999). Therefore, high O_β ratio is indicative of superior
236 SCR activity. After doping K_3PO_4, the ratio of $O_\beta/(O_\alpha+O_\beta+O_\gamma)$ was found to decrease
237 from 0.35 to 0.23, which indicated less surface chemisorbed oxygen on the surface of
238 K_3PO_4–doped CT. This might be due to the fact that potassium ions easily occupied
239 oxygen vacancies since they had similar ionic radius with oxygen ions (Zhang *et al.*,
240 2014). These results confirmed that the decrease of Ce^{3+} was accompanied by the

241 decrease in oxygen vacancies and active oxygen species, which played a negative role
242 in the SCR activity of CT.
243 3.2.4 NH_3–TPD results
244 NH_3–TPD analysis was performed to study the effect of K_3PO_4 on the surface
245 acidity of CT and the results are shown in Fig. 8. The fresh CT exhibited a broad NH_3
246 desorption peak spanned in the temperature range of 100–500 °C and a small peak at
247 500–700 °C. After deconvolution and peak–fitting, the broad peak could be separated
248 into two peaks centered at about 205 °C and 310 °C. It is known that the ammonia
249 adsorbed on Brønsted acid sites has less thermal stability than that adsorbed on Lewis
250 acid sites during TPD process (Phil *et al.*, 2008). As a result, the low– and
251 medium–temperature peaks could be assigned to the weak and moderate adsorption of
252 ammonia on Brønsted acid sites (Cai *et al.*, 2014). The small high–temperature peak
253 could be attributed to the NH_3 species strongly adsorbed on Lewis acid sites (Zhao *et*
254 *al.*, 2016; Duan *et al.*, 2017). It was clear that most of adsorbed NH_3 was coordinated
255 to Brønsted acid sites, which played a predominant role in SCR reaction. After doping
256 K_3PO_4, no significant change was observed on the high–temperature NH_3 desorption
257 peak. This indicated that the Lewis acid sites on the surface of CT were hardly
258 influenced by K_3PO_4. However, the other two peaks shifted to lower temperatures,
259 while their peak areas decreased considerably, especially the medium–temperature
260 peak. Tang *et al*. (2010) also found similar changes on the NH_3–TPD profiles of
261 Na^+–V_2O_5/TiO_2 catalysts. It is accepted that the peak location is closely related to the
262 adsorption strength and the peak area corresponds to the amount of the adsorbed NH_3

(Cai *et al.*, 2014). After doping K_3PO_4, though the NH_3 adsorbed species could be more easily desorbed at low temperatures, the tremendous decrease in the Brønsted acidity resulted in the great weakness of the ability of CT to adsorb NH_3. Ce^{3+} was reported to be related to the formation of Brønsted acid sites (Shu *et al.*, 2012). It would be worthwhile to notice that the decrease in the amount of Ce^{3+} on the surface of K_3PO_4–doped CT had been demonstrated by the above XPS results. Therefore, the significant decrease in the amount of Brønsted acid sites is one of the main reasons for the loss of the activity of CT after doping with K_3PO_4.

3.2.5 H_2–TPR results

Fig. 9 displays the H_2–TPR profiles of the fresh and K_3PO_4–doped CT catalysts. As for the fresh CT, the onset temperature of reduction was at about 320 °C and there were two overlapped reduction peaks centered at around 515 °C and 680 °C. The peak at low temperature was probably related to the reduction of the surface oxygen of ceria (Ce^{4+}–O–Ce^{4+}) and the one at high temperature could be attributed to the reduction of Ce^{4+} to Ce^{3+} (Liu *et al.*, 2013b; Liu *et al.*, 2018). In contrast, the onset temperature of reduction shifted to a higher value (about 370 °C) and only one reduction peak centered at about 600 °C was observed over KPCT(0.5). Higher onset and reduction peak temperatures are generally regarded as indicators of the decrease in the reducibility (Liu *et al.*, 2008; Gao *et al.*, 2010; Zhao *et al.*, 2016). It was clear that the presence of K_3PO_4 led to the remarkable drop in the reducibility of CT. It should be noted that this result was exactly in line with that of the above XPS analysis. In correlation with the results of BET, XRD and XPS, the loading of K_3PO_4 made CT

reduced harder probably because of decreased surface area, less surface oxygen, change in chemical state of Ce species and the interaction of K_3PO_4 with Ce species.

4. Conclusions

K_3PO_4 seriously deactivated Ce–Ti oxide catalyst for the selective catalytic reduction of NO with NH_3. The fresh and K_3PO_4–doped Ce–Ti oxides were characterized using XRD, BET, XPS, H_2–TPR and NH_3–TPD. The results indicated that K_3PO_4 had no significant effect on the dispersion and crystalline form of Ce species on anatase TiO_2. The BET surface area and total pore volume was found to decrease and there was slight pore blocking after doping K_3PO_4. XPS results revealed that the interaction between K_3PO_4 and Ce species hindered the transformation of Ce^{4+} to Ce^{3+}. As a result, the amount of Ce^{3+} deceased, accompanied by a decrease of oxygen vacancies and active oxygen species. These played a negative role in the SCR reaction over Ce–Ti oxide. Both XPS and H_2–TPR results demonstrated the degradation of the reducibility of Ce–Ti oxide after doping K_3PO_4. In addition, the reduction in surface acidity mainly due to the decrease in the amount of Brønsted acid sites could lead to the marked drop in the amount of NH_3 absorbed on the catalyst surface. On the basis of these results, the decrease in the amount of Ce^{3+}, oxygen vacancies and surface chemisorbed oxygen and the degradation of surface Brønsted acidity and reducibility were primarily responsible for the deactivation by K_3PO_4 of Ce–Ti oxide.

Acknowledgements

This work was supported by the National Natural Science Foundation of China (No. 51506226), Natural Science Foundation of Shandong Province (No. ZR2015EM010), "the Fundamental Research Funds for the Central Universities" (No. 15CX05005A) and the scholarship from China Scholarship Council, China (CSC) (No. 201706455013).

Reference

Beck, J., Brandenstein, J., Unterberger, S., Hein, K.R.G. (2004). Effects of sewage sludge and meat and bone meal Co–combustion on SCR catalysts. *Appl. Catal. B Environ.* 49: 15–25.

Burroughs, P., Hamnett, A., Orchard, A.F. and Thornton, G. (1976). Satellite structure in the X–ray photoelectron spectra of some binary and mixed oxides of lanthanum and cerium. *J. Chem. Soc. Dalton. Trans.* 17: 1686–1698.

Cai, S., Zhang, S., Zhang, L., Huang, L., Li, H., Gao, R., Shi, L., Zhang, J. (2014). Comparative study of 3D ordered macroporous $Ce_{0.75}Zr_{0.2}M_{0.05}O_{2-\delta}$ (M=Fe, Cu, Mn, Co) for selective catalytic reduction of NO with NH_3. *Catal. Sci. Technol.* 4: 93–101.

Castellino, F., Jensen, A.D., Johnsson, J.E., Fehrmann, R. (2009). Influence of reaction products of K–getter fuel additives on commercial vanadia–based SCR catalysts: Part I. Potassium phosphate. *Appl. Catal. B Environ* 86: 196–205.

Chen, L., Li, J., Ge, M. (2009). Promotional effect of Ce–doped V_2O_5–WO_3/TiO_2

with low vanadium loadings for selective catalytic reduction of NO_x by NH_3. *J. Phys. Chem. C* 113: 21177–21184.

Chen, L., Li, J., Ge, M. (2011). The poisoning effect of alkali metals doping over nano V_2O_5–WO_3/TiO_2 catalysts on selective catalytic reduction of NO_x by NH_3. *Chem. Eng. J.* 170: 531–537.

Chen, Y., Wang, M., Du, X., Ran, J., Zhang, L., Tang, D. (2018). High resistance to Na poisoning of V_2O_5–$Ce(SO_4)_2/TiO_2$ catalyst for the NO SCR reaction. *Aerosol Air Qual. Res.* DOI: 10.4209/aaqr.2017.11.0521.

Du, X., Gao, X., Qu, R., Ji, P., Luo, Z., Cen, K. (2012). The influence of alkali metals on the Ce–Ti mixed oxide catalyst for the selective catalytic reduction of NO_x. *ChemCatChem* 4: 2075–2081.

Du, X., Xue, J., Wang, X., Chen, Y., Ran, J. and Zhang, L. (2018). Oxidation of Sulfur Dioxide over V_2O_5/TiO_2 Catalyst with Low Vanadium Loading: A Theoretical Study. *J. Phys. Chem. C* 122: 4517–4523.

Du, X., Yang, G., Chen, Y., Ran, J., Zhang, L. (2017). The different poisoning behaviors of various alkali metal containing compounds on SCR catalyst. *Appl. Surf. Sci.* 392: 162–168.

Duan, Z., Chi, K., Liu, J., Shi, J., Zhao, Z., Wei, Y., Song, W. (2017). The catalytic performances and reaction mechanism of nanoparticle Cd/Ce–Ti oxide catalysts for NH_3–SCR reaction. *RSC Adv.* 7: 50127–50134.

Dunn, J.P., Koppula, P.R., Stenger, H.G. and Wachs I.E. (1998). Oxidation of sulfur dioxide to sulfur trioxide over supported vanadia catalysts. *Appl. Catal. B* 19:

103–117.

Dupin, J.C., Gonbeau, D., Vinatier, P. and Levasseur, A. (2000). Systematic XPS studies of metal oxides, hydroxides and peroxides. *Phys. Chem. Chem. Phys.* 2: 1319–1324.

Eom, Y., Jeon, S.H., Ngo, T.A., Kim, J. and Lee, T.G. (2008). Heterogeneous mercury reaction on a selective catalytic reduction (SCR) catalyst. *Catal. Lett.* 121: 219–225.

Fedeyko, J.M., Chen, B, Chen, H. (2010). Mechanistic study of the low temperature activity of transition metal exchanged zeolite SCR catalysts. *Catal. Today* 151: 231–236.

Gao, S., Wang, P., Chen, X., Wang, H., Wu, Z., Li, Y. (2014). Enhanced alkali resistance of CeO_2/SO_4^{2-}–ZrO_2 catalyst in selective catalytic reduction of NO_x by ammonia. *Catal. Commun.* 43: 223–226.

Gao, X., Jiang, Y., Fu, Y., Zhong, Y., Luo, Z., Cen, K. (2010). Preparation and characterization of CeO_2/TiO_2 catalysts for selective catalytic reduction of NO with NH_3. *Catal. Commun.* 11: 465–469.

Geng, Y., Chen, X., Yang, S., Liu, F., Shan, W. (2017). Promotional effects of Ti on a CeO_2–MoO_3 catalyst for the selective catalytic reduction of NO_x with NH_3. *Appl. Mater. Interfaces* 9: 16951–16958.

Guo, R., Zhou, Y., Pan, W., Hong, J., Zheng, W., Jin, Q., Ding, C. and Guo. S. (2013). Effect of preparation methods on the performance of CeO_2/Al_2O_3 catalysts for selective catalytic reduction of NO with NH_3. *J. Ind. Eng. Chem.* 19: 2022–2025.

372 Jang, H., Kim, J., Back, S., Sung, J., Yoo, H., Choi, H.S., Seo, Y. (2016). Combustion
373 characteristics of waste sludge at air and oxy–fuel combustion conditions in a
374 circulating fluidized bed reactor. *Fuel* 170: 92–99.
375 Jiang, Y., Bao, C., Liu, S., Liang, G., Lu, M., Lai, C., Shi, W., Ma, S. (2018).
376 Enhanced activity of Nb–modified CeO_2/TiO_2 catalyst for the selective catalytic
377 reduction of NO with NH_3. *Aerosol Air Qual. Re*s. 18: 2121–2130
378 Jiang, Y., Gao, X., Zhang, Y., Wu, W., Song, H., Luo, Z., Cen, K. (2014). Effects of
379 $PbCl_2$ on selective catalytic reduction of NO with NH_3 over vanadia–based
380 catalysts. *J. Hazard. Mater.* 274: 270–278.
381 Jiang, Y., Wang, X., Xing, Z., Bao, C., Liang, G. (2017a). Preparation and
382 characterization of CeO_2–MoO_3/TiO_2 catalysts for selective catalytic reduction of
383 NO with NH_3. *Aerosol Air Qual. Res.* 17: 2726–2734.
384 Jiang, Y., Wang, X., Bao, C., Huang, S., Zhang, X., Wang, X. (2017b). Poisoning
385 effect of CaO on CeO_2/TiO_2 catalysts for selective catalytic reduction of NO with
386 NH_3. *Korean J. Chem. Eng.* 34: 1874–1881.
387 Lee, T., Bai, H. (2018). Metal Sulfate Poisoning effects over $MnFe/TiO_2$ for selective
388 catalytic reduction of NO by NH_3 at low temperature. *Ind. Eng. Chem. Res.* 57:
389 4848–4858.
390 Leofantia, G., Padovanb, M., Tozzolac, G., Venturellic, B. (1998). Surface area and
391 pore texture of catalysts. *Catal. Today* 41: 207–219.
392 Li, Q., Liu, H., Chen, T., Chen, D., Zhang, C., Xu, B., Zhu, C., Jiang, Y. (2017).
393 Characterization and SCR performance of nano–structured iron–manganese oxides:

394 Effect of annealing temperature. *Aerosol Air Qual. Res.* 17: 2328–2337.

395 Liu, C., Chen, L., Chang, H., Ma, L., Peng, Y., Arandiyan, H., Li, J. (2013b).
396 Characterization of CeO_2–WO_3 catalysts prepared by different methods for
397 selective catalytic reduction of NO_x with NH_3. *Catal. Commun.* 40: 145–148.

398 Liu, J., Zhao, Z., Wang, J., Xu, C., Duan, A., Jiang, G., Yang, Q. (2008). The highly
399 active catalysts of nanometric CeO_2–supported cobalt oxides for soot combustion,
400 *Appl. Catal. B Environ.* 84: 185–195.

401 Liu, Z., Feng, X., Zhou, Z., Feng, Y., Li, J. (2018). Ce–Sn binary oxide catalyst for the
402 selective catalytic reduction of NO_x by NH_3. *Appl. Surf. Sci.* 428: 526–533.

403 Liu, Z., Yi, Y., Li, J., Woo, S.I., Wang, B., Cao, X., Li, Z. (2013a). A superior catalyst
404 with dual redox cycles for the selective reduction of NO_x by ammonia. *Chem.*
405 *Commun.* 49: 7726–7728.

406 Long, R.; Yang, R.T. (1999). Catalytic Performance of Fe–ZSM–5 catalysts for
407 selective catalytic reduction of nitric oxide by ammonia. *J. Catal.* 188: 332–339.

408 Ma, Z., Yang, H., Liu, F., Zhang, X. (2013). Interaction between SO_2 and
409 Fe–Cu–O_x/CNTs–TiO_2 catalyst and its influence on NO reduction with NH_3. *Appl.*
410 *Catal. A Chem.* 467: 450–455.

411 Peng, Y., Li, J., Chen, L., Chen, J., Han, J., Zhang, H., Han, W. (2012). Alkali metal
412 poisoning of a CeO_2–WO_3 catalyst used in the selective catalytic reduction of NO_x
413 with NH_3: an experimental and theoretical study. *Environ. Sci. Technol.* 46:
414 2864–2869.

415 Phil, H.H., Reddy, M.P., Kumar, P.A., Ju, L.K., Hyo, J.S. (2008). SO_2 resistant

antimony promoted V_2O_5/TiO_2 catalyst for NH_3–SCR of NO_x at low temperatures. *Appl. Catal. B Environ.* 78: 301–308.

Shu, Y., Sun, H., Quan, X., Chen, S. (2012). Enhancement of catalytic activity over the iron–modified Ce/TiO_2 catalyst for selective catalytic reduction of NO_x with ammonia. *J. Phys. Chem. C* 116: 25319–25327.

Tang, F., Xu, B., Shi, H., Qiu, J., Fan, Y. (2010). The poisoning effect of Na^+ and Ca^{2+} ions doped on the V_2O_5/TiO_2 catalysts for selective catalytic reduction of NO by NH_3. *Appl. Catal. B Environ.* 94: 71–76.

Wagner, C.D., Riggs, W.M., Davis, L.E., Moulder, J.F. and Mullenberg, G.E. (1979). Handbook of X–ray Photoelectron Spectroscopy, Perkin–Elmer Corporation, Minnesota.

Wang, H., Chen, X., Gao, S., Wu, Z., Liu, Y., Weng, X. (2013). Deactivation mechanism of Ce/TiO_2 selective catalytic reduction catalysts by the loading of sodium and calcium salts. *Catal. Sci. Technol.* 3: 715–722.

Wang, S., Guo, R., Pan, W., Chen, Q., Sun, P., Li, M., Liu, S. (2017). The deactivation of Ce/TiO_2 catalyst for NH_3–SCR reaction by alkali metals: TPD and DRIFT studies. *Catal. Commun.* 89: 143–147.

Wang, X., Du, X., Zhang, L., Chen, Y., Yang, G., Ran, J. (2018). Promotion of NH_4HSO_4 decomposition in NO/NO_2 contained atmosphere at low temperature over V_2O_5–WO_3/TiO_2 catalyst for NO reduction. *Appl. Catal. A* 559: 112–121.

Wu, Z., Jin, R., Liu, Y. and Wang, H. (2008). Ceria modified MnO_x/TiO_2 as a superior catalyst for NO reduction with NH_3 at low–temperature. *Catal. Commun.* 9:

438 2217–2210.

439 Yates, M., Martín, J.A., Martín–Luengo, M.Á., Suárez, S. and Blanco, J. (1996). N_2O
440 formation in the ammonia oxidation and in the SCR process with V_2O_5–WO_3
441 catalysts. *Catal. Today* 107–108: 120–125.

442 Yu, X., Cao, F., Zhu, X., Zhu, X., Gao, X., Luo, Z., Cen, K. (2017). Characterization
443 and SCR performance of nano–structured iron–manganese oxides: Effect of
444 annealing temperature. *Aerosol Air Qual. Res.* 17: 302–313.

445 Zhang, L., Cui, S., Guo, H., Ma, X., Luo, X. (2014). The influence of K^+ cation on the
446 MnO_x–CeO_2/TiO_2 catalysts for selective catalytic reduction of NO_x with NH_3 at
447 low temperature. *J. Mol. Catal., A* 390: 14–21.

448 Zhang, L., Cui, S., Guo, H., Ma, X., Luo, X. (2015). The poisoning effect of
449 potassium ions doped on MnO_x/TiO_2 catalysts for low–temperature selective
450 catalytic reduction. *Appl. Surf. Sci.* 355: 1116–1122.

451 Zhao, K., Han, W., Lu, G., Lu, J., Tang, Z. and Zhen. X. (2016). Promotion of redox
452 and stability features of doped Ce–W–Ti for NH_3–SCR reaction over a wide
453 temperature range. *Appl. Surf. Sci.* 379: 316–322.

454 Zhuo, J., Li, S., Duan, L., Yao, Q. (2012). Effect of phosphorus transformation on the
455 reduction of particulate matter formation during Co–combustion of coal and
456 sewage sludge. *Energy Fuels* 26: 3162–3166.

457

458 **Figure captions**

459 **Fig. 1** Variation of NO conversion with temperatures over Ce–Ti oxides doped with
460 different P species. Reaction condition: [NO]=[NH_3]=1,000 ppm, [O_2]=3%, N_2
461 balance, total flow rate=500 ml/min, and GHSV=90,000 h^{-1}.

462 **Fig. 2** Variation of NO conversion with temperatures over Ce–Ti oxides with different
463 K_3PO_3 loadings. Reaction condition: [NO]=[NH_3]=1,000 ppm, [O_2]=3%, N_2 balance,
464 total flow rate=500 ml/min, and GHSV=90,000 h^{-1}.

465 **Fig. 3** Oxidation of NO to NO_2 by O_2 over CT and KPCT(0.5). Reaction condition:
466 [NO]=1,000 ppm, [O_2]=3%, N_2 balance, total flow rate =500 ml/min, and
467 GHSV=90,000 h^{-1}.

468 **Fig. 4** NO formation over CT and KPCT(0.5). Reaction condition: [NH_3]=1,000 ppm,
469 [O_2]=3%, N_2 balance, total flow rate =500 ml/min, and GHSV=90,000 h^{-1}.

470 **Fig. 5** XRD patterns of Ce–Ti oxides with different K_3PO_3 loadings.

471 **Fig. 6** N_2 adsorption–desorption isotherms (a) and pore size distribution curves (b) of
472 CT and KPCT(0.5).

473 **Fig. 7** XPS spectra of K 2p (a), Ti 2p (b), Ce 3d (c) and O 1s (d) of CT and
474 KPCT(0.5).

475 **Fig. 8** NH_3–TPD profiles of CT and KPCT(0.5).

476 **Fig. 9** H_2–TPR profiles of CT and KPCT(0.5).

Fig. 1

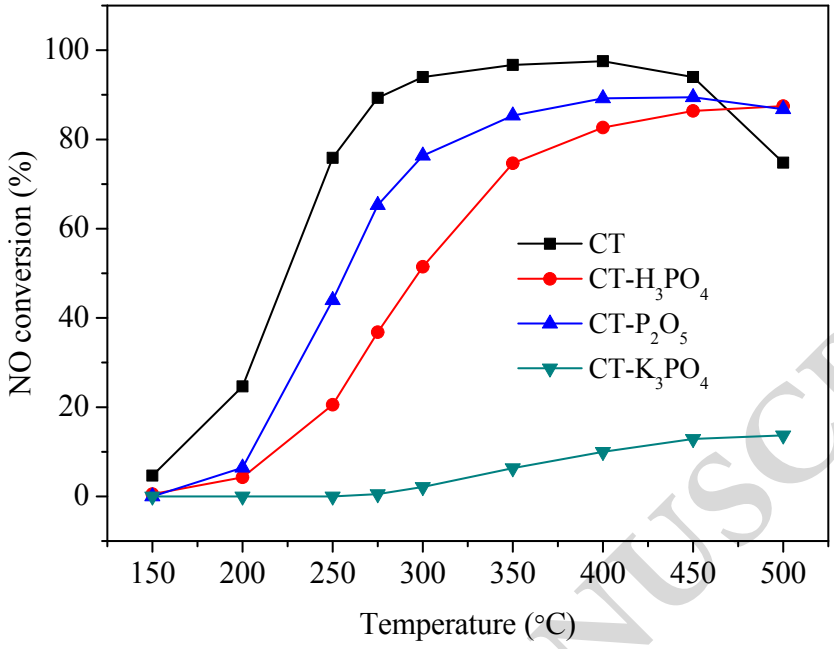

Fig. 2

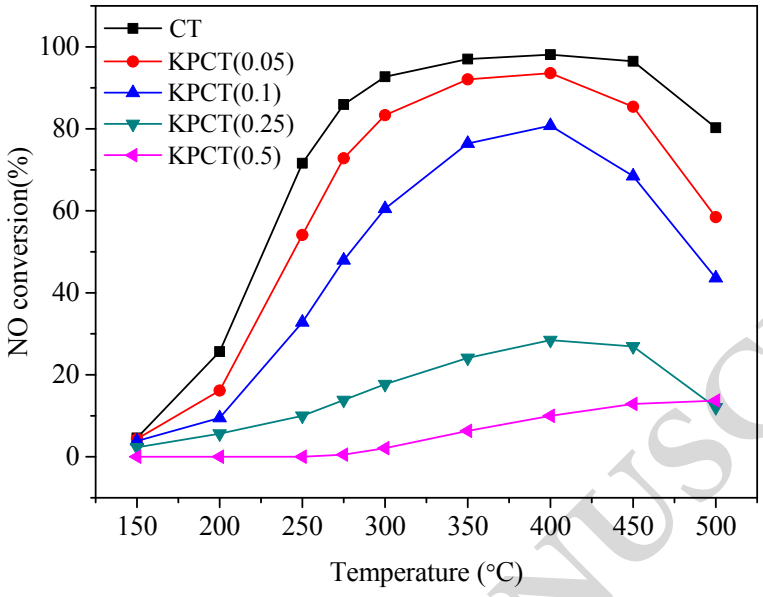

Fig. 3

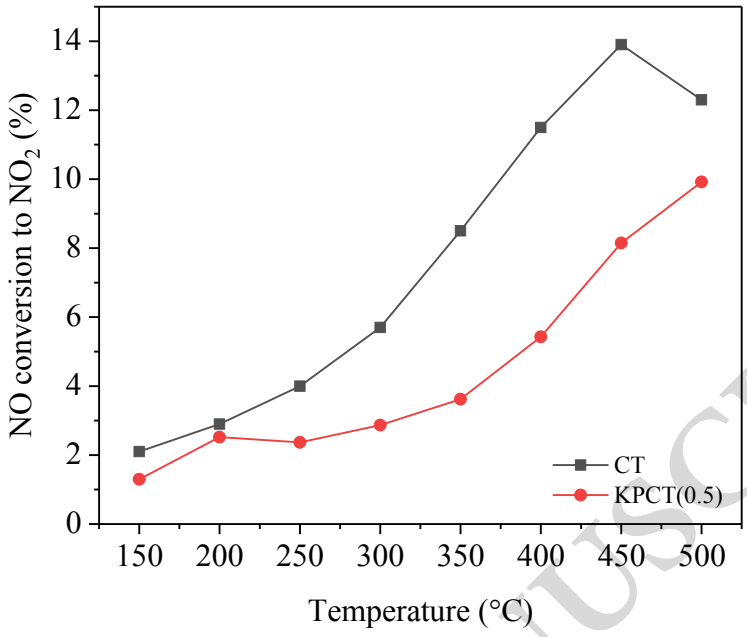

Fig. 4

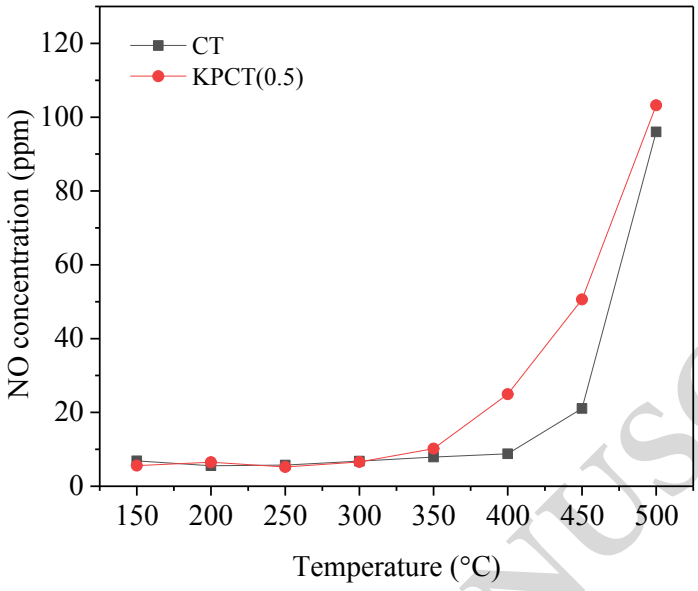

Fig. 5

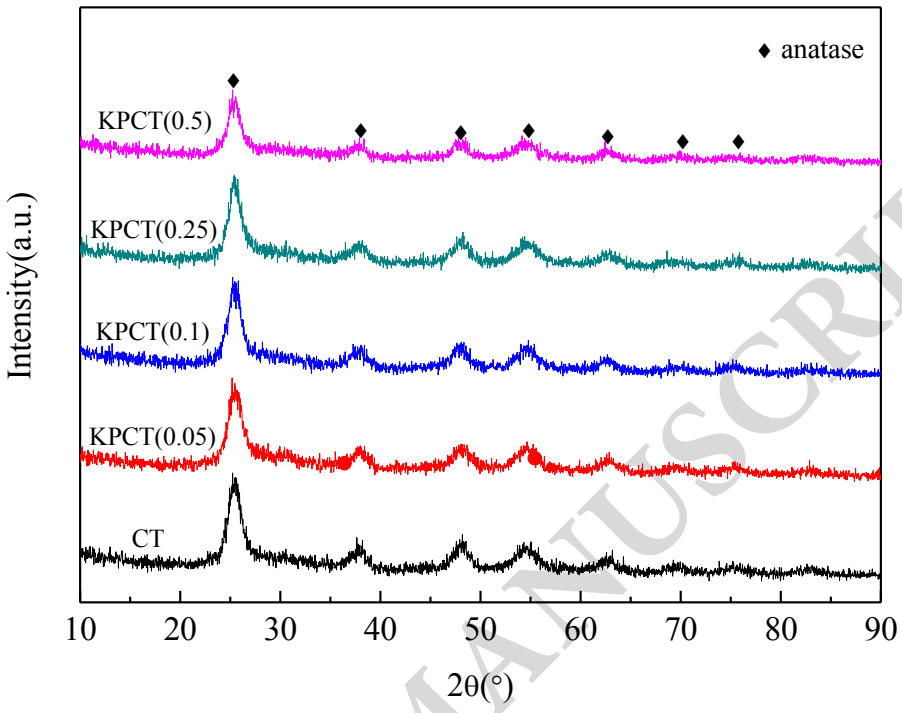

Fig. 6

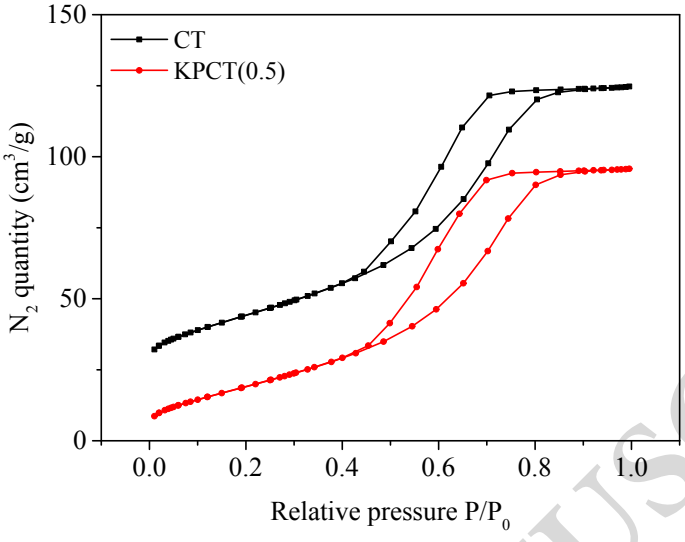

(a)

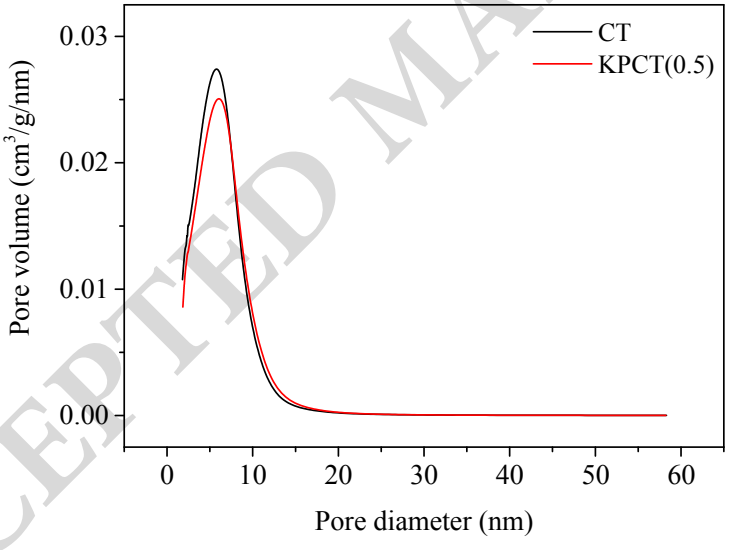

(b)

Fig. 7

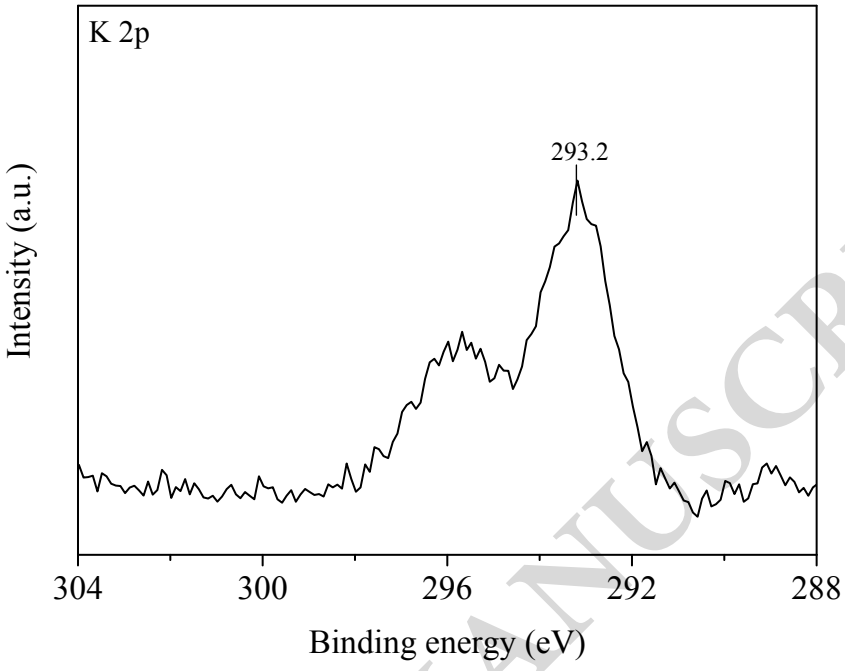

(a)

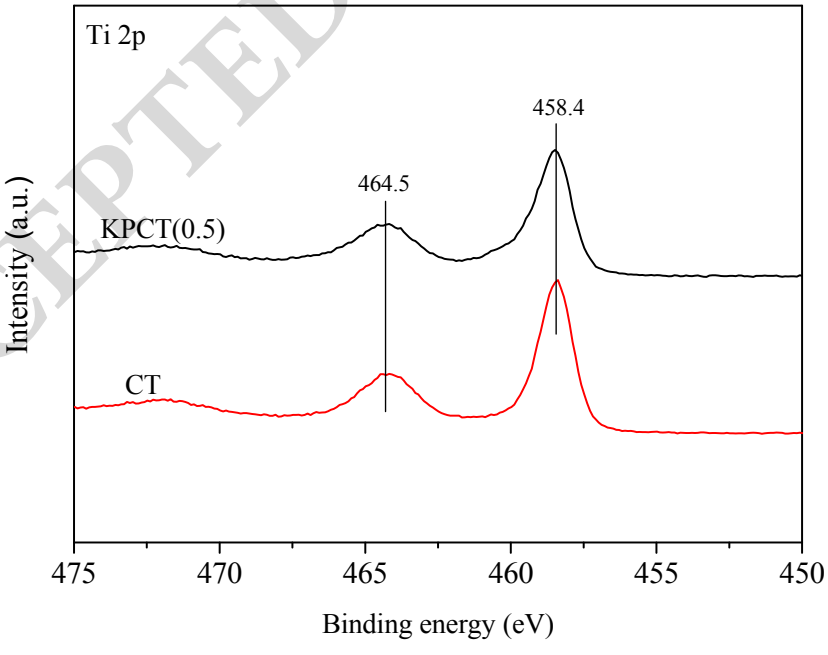

(b)

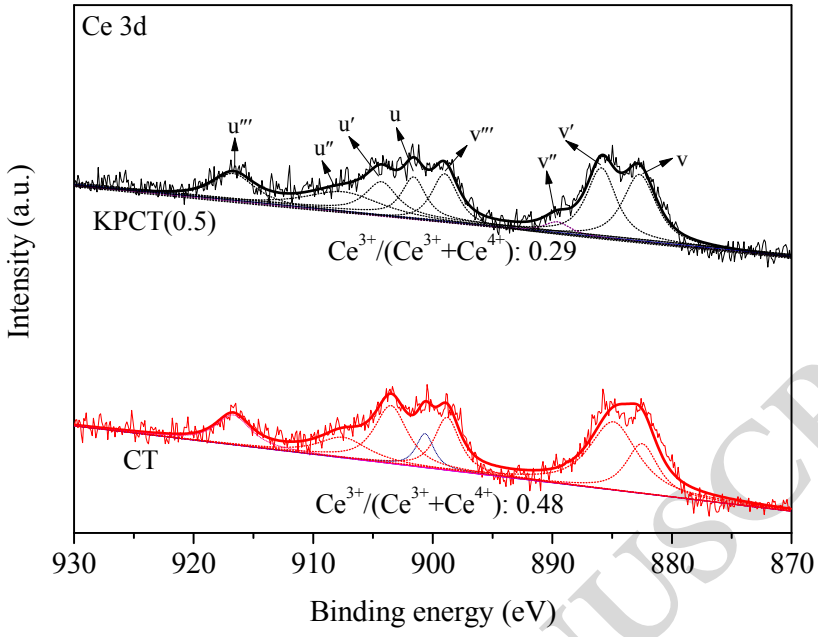

(c)

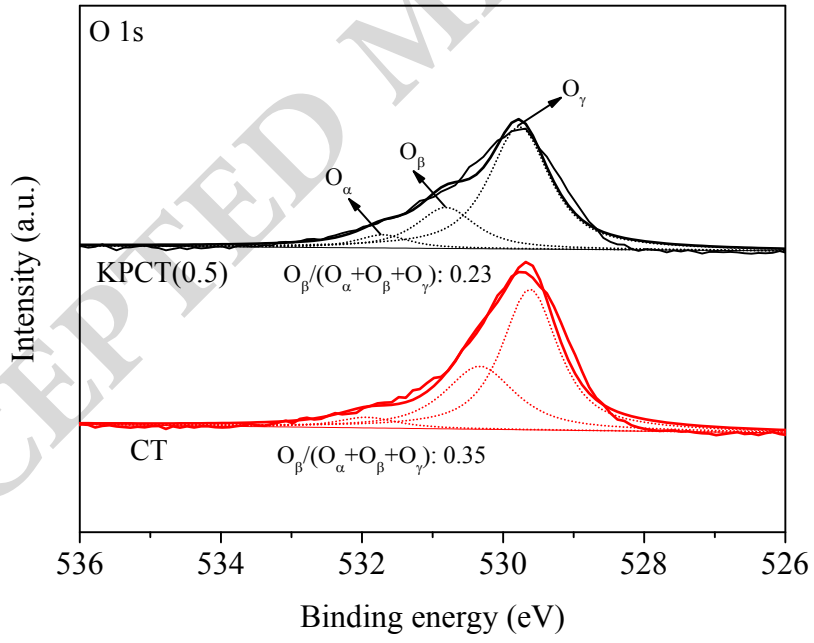

(d)

Fig. 8

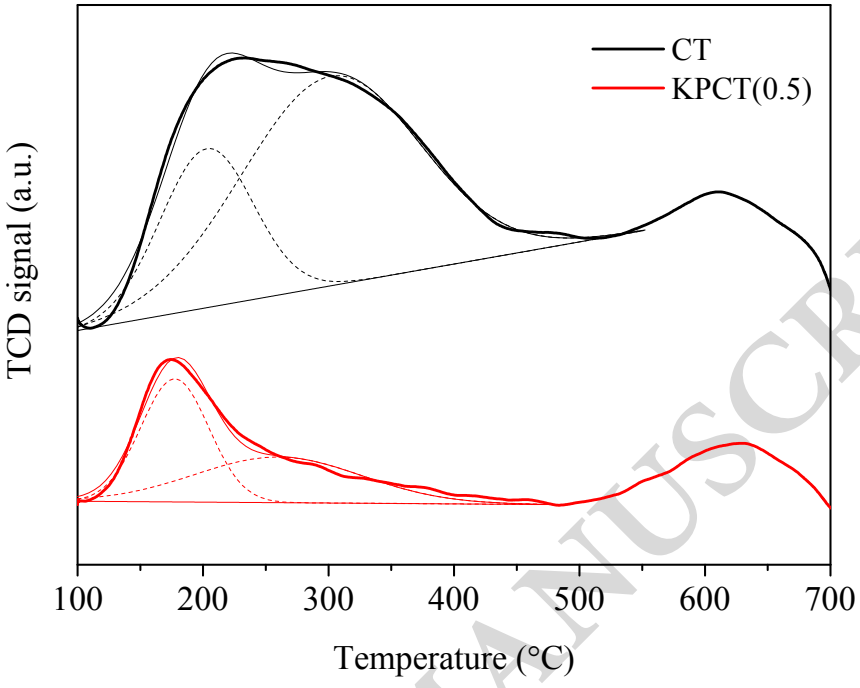

Fig. 9

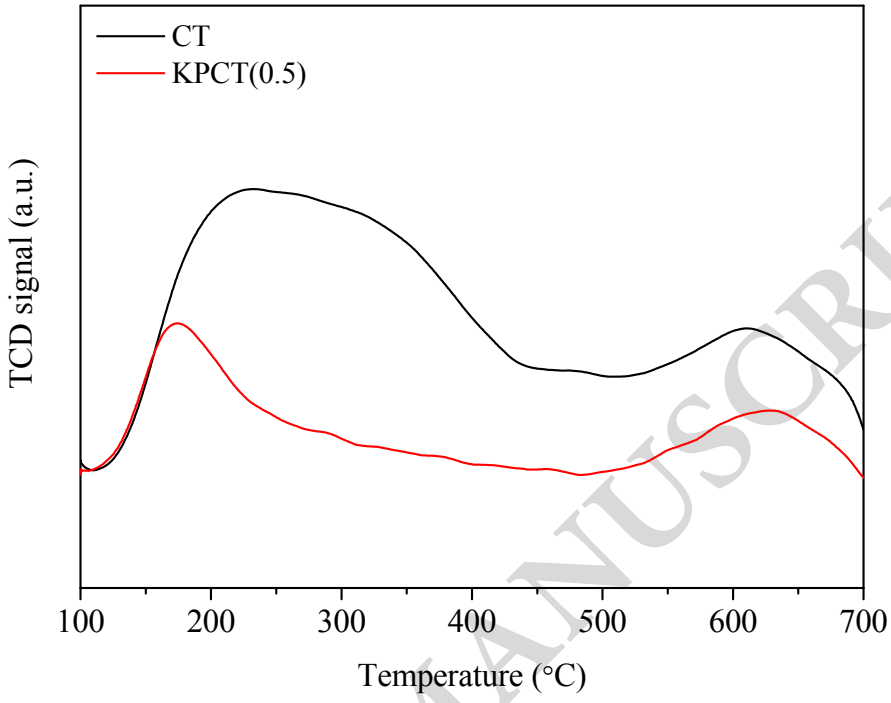

Table 1 Surface atomic concentration of different elements on fresh and K_3PO_4-doped CT catalysts

Samples	Surface atomic concentration (at. %)				
	Ce	Ti	O	P	K
CT	30.53	34.43	31.52	-	-
KPCT(0.5)	30.18	32.80	31.43	0.63	3.60